Diffusion-Enhanced Visualization and Quantification of Vascular Anomalies in Three-Dimensional Rotational Angiography: Results of an In-Vitro Evaluation

Erik Meijering, Wiro Niessen, Joachim Weickert, Max Viergever

Medical Image Analysis, vol. 6, no. 3, September 2002, pp. 215–233

Abstract—Three-dimensional rotational angiography (3DRA) is a new and promising technique for obtaining high-resolution isotropic 3D images of vascular structures. However, due to the relatively high noise level and the presence of other background structures in clinical 3DRA images, noise reduction is inevitable. In this paper, we evaluate a number of linear and nonlinear diffusion techniques for this purpose. Specifically, we analyze the effects of these techniques on the threshold-based visualization and quantification of vascular anomalies in 3DRA images. The results of in-vitro experiments indicate that edge-enhancing anisotropic diffusion filtering is most suitable: the increase in the user-dependency of visualizations and quantifications is considerably less with this technique compared to linear filtering techniques, and it is better at reducing noise near edges than isotropic nonlinear diffusion. However, in view of the memory and computation-time requirements of this technique, the latter scheme may be considered a useful alternative.

Keywords—Three-dimensional rotational angiography, noise reduction, linear diffusion, isotropic nonlinear diffusion, edge-enhancing anisotropic diffusion, in-vitro evaluation.

1 Introduction

Three-dimensional rotational angiography (3DRA) is a relatively new technique for imaging blood vessels in the human body, which has the potential to overcome some of the limitations and drawbacks of conventional two-dimensional (2D) projective X-ray angiography. With the latter type of imaging, projections from different angles are often required in order to substantiate the accuracy of diagnostic findings, such as *e.g.* the precise location, size, and morphology of arterial stenoses and aneurysms [6, 18, 34, 71]. This does not only result in prolonged examination times, and hence prolonged exposure to X-rays, but also requires multiple injections of contrast material, which altogether significantly increase the discomfort for the patient.

With 3DRA, on the other hand, the same C-arm imaging system is used to acquire a sequence of about one hundred low-dose X-ray angiography images during a 180-degree rotation of the X-ray source-detector combination, following a single injection of contrast material. Application of a subsequent reconstruction algorithm to the images results in high-resolution 3D isotropic datasets of the vascular structures of interest, which can afterwards be studied interactively and from any desired angle by the use of 3D visualization techniques [2,20,30,48,64,72]. The absence of overprojections and the high resolution of the resulting datasets make the technique also potentially interesting for quantitative studies.

However, visualization of raw clinical 3DRA datasets usually does not yield satisfactory results, due to the relatively high noise level and the presence of other background structures resulting from inhomogeneous surrounding tissue. In order to improve the quality of the renderings, some form of noise reduction must be applied to the original data prior to visualization. In the 3DRA visualization software used in our institute, this is currently done by simple uniform filtering. Although application of noise reduction techniques is generally found to result in qualitatively better renderings, the effects of such techniques on the quantification of vessels and their anomalies based on those renderings have, to our knowledge, not yet been reported in the literature, save for a recently published conference paper by the present authors [46]. Analysis of these effects is important, as particular techniques may influence the user-dependency of the renderings—which in general rely on one or more user-defined thresholds—and thus the reliability of quantitative measurements based on them.

In this paper we present the results of a study into the effects of several linear and nonlinear noise reduction techniques on the accuracy of quantification and the quality of visualization of vascular anomalies in 3DRA images. A brief description of the techniques included in this study is given in Section 2, followed by a discussion of the vascular anomalies and the measurements involved in their quantification in Section 3. The materials and methods used in the in-vitro experiments are described in Section 4. The results of these experiments are presented in Section 5, and discussed in Section 6. Concluding remarks are made in Section 7.

2 Noise Reduction Techniques

Noise reduction techniques can be divided into linear and (adaptive) nonlinear techniques. Concerning the former, we limited ourselves to uniform and Gaussian filtering. The nonlinear filtering techniques included in this study were regularized isotropic nonlinear diffusion and edge-enhancing anisotropic diffusion. We briefly describe each of them.

2.1 Uniform Filtering

The simplest and computationally cheapest approach to reduce noise in images is to average the grey-values of voxels in a cubic neighborhood around each voxel. This can be implemented by means of separable uniform filtering (UF), also known as neighborhood averaging [29] or box filtering [37]:

$$I(\mathbf{x}) = (I_0 * U_m)(\mathbf{x}), \quad \mathbf{x} = (x, y, z) \in X, \tag{1}$$

where I_0 denotes the original 3D image, $X \subset \mathbb{R}^3$ is the image domain, and U_m denotes the 3D normalized uniform filter given by

$$U_m(\mathbf{x}) = u_m(x)u_m(y)u_m(z), \tag{2}$$

with $u_m : \mathbb{R} \to \mathbb{R}$ defined as

$$u_m(\xi) \triangleq \begin{cases} 1/m, & \text{if } |\xi| \leqslant m/2 \\ 0, & \text{otherwise.} \end{cases} \tag{3}$$

In these equations, the parameter m determines the support of the uniform filter, which, in principle, can have any real value larger than zero. When dealing with discrete data,

however, the possible values of m are effectively limited to odd integers, in which case this parameter indicates the number of voxels in each dimension involved in the averaging.

The noise reduction capability of UF is explained from the fact that U_m is a low-pass filter; its Fourier transform can easily be derived to be

$$\tilde{U}_m(\mathbf{f}) = \operatorname{sinc}(mf_x)\operatorname{sinc}(mf_y)\operatorname{sinc}(mf_z), \tag{4}$$

where $\mathbf{f} = (f_x, f_y, f_z) \in \mathbb{R}^3$ denotes spatial frequency.

2.2 Gaussian Filtering

Another frequently used approach to image smoothing is Gaussian filtering (GF). Similar to UF, it can be implemented by separable convolution:

$$I(\mathbf{x}) = (I_0 * G_\sigma)(\mathbf{x}), \quad \mathbf{x} = (x, y, z) \in X, \tag{5}$$

where G_σ denotes the 3D Gaussian filter with standard deviation σ, given by

$$G_\sigma(\mathbf{x}) = g_\sigma(x)g_\sigma(y)g_\sigma(z), \tag{6}$$

with $g_\sigma : \mathbb{R} \to \mathbb{R}$ defined as

$$g_\sigma(\xi) \triangleq \frac{1}{\sigma\sqrt{2\pi}} \exp\left(\frac{-\xi^2}{2\sigma^2}\right). \tag{7}$$

The ubiquitousness of the Gaussian convolution kernel in digital image processing applications is explained by the fact that it possesses some important properties: application of this kernel does not create spurious details and the result is independent of the location and orientation of image structures [40]. These are essential requirements for the purpose of segmentation and analysis of image structures. For more details on these and other properties of the Gaussian kernel, we refer to several books on scale-space theory in computer vision [24, 42, 68].

The noise reduction capability of GF can be explained in the frequency domain by the fact that G_σ is a low-pass filter; its Fourier transform is also a Gaussian, of the form

$$\tilde{G}_\sigma(\mathbf{f}) = \exp\Big(-2\pi^2\sigma^2\big(f_x^2 + f_y^2 + f_z^2\big)\Big). \tag{8}$$

In the spatial domain, the smoothing effect of GF follows from the observation that (5) constitutes the solution to the diffusion equation [40], or heat conductance equation:

$$\begin{aligned} \partial_t I(\mathbf{x}; t) &= \operatorname{div}(\nabla I)(\mathbf{x}; t), \\ I(\mathbf{x}; 0) &= I_0(\mathbf{x}), \end{aligned} \tag{9}$$

provided that $\sigma = \sqrt{2t}$. The linear diffusion process governed by (9) is known to gradually destroy all image structure and eventually result in a homogeneous image with intensity equal to the mean of the original image.

2.3 Regularized Isotropic Nonlinear Diffusion

In order to better preserve edges while reducing noise, a smoothing algorithm should take into account local image contrast. For this purpose, several nonlinear diffusion schemes have been proposed [70, 76, 77]. In the present study, we included the scheme originally due

to Perona & Malik [56] and refined by Catté *et al.* [8]. This so called regularized isotropic nonlinear diffusion scheme—in the sequel referred to as regularized Perona-Malik diffusion (RPM)—is obtained by modifying (9) so as to include a gradient-dependent diffusivity:

$$\partial_t I(\mathbf{x};t) = \operatorname{div}\bigl(D\bigl(\|\nabla I_\tau\|^2\bigr)\nabla I\bigr)(\mathbf{x};t), \tag{10}$$

where the gradient magnitude is computed at scale $\sigma_n = \sqrt{2\tau}$, $\tau > 0$. This noise-scale parameter makes the filter insensitive to noise at scales smaller than σ_n, and also serves as a regularization parameter that guarantees well-posedness of the process [8, 77].

In order to achieve intra-regional smoothing while avoiding smoothing across object boundaries, the diffusivity D must be a monotonic function such that $D \to 1$ when the gradient magnitude is small and $D \to 0$ when it is large. In our implementation, we used the following diffusivity [77, 79, 80]:

$$D\bigl(\xi^2\bigr) = 1 - \exp\left(\frac{-C}{(\xi/\zeta)^8}\right), \tag{11}$$

where $\zeta > 0$ acts as a "contrast" parameter: structures with $\|\nabla I_\tau\| > \zeta$ are regarded as edges, for which $D \to 0$ and hence diffusion is inhibited, while structures with $\|\nabla I_\tau\| < \zeta$ are assumed to belong to the interior of a region, for which $D \to 1$ and hence (10) approaches the linear diffusion equation (9). The constant C must be chosen such that the flux function $\xi\, D(\xi^2)$, the derivative of which determines whether (10) describes forward or backward diffusion, is increasing for $\xi \in [0, \zeta]$ and decreasing for $\xi \in (\zeta, \infty)$. This implies [77, 79] that $C \approx 3.31488$.

2.4 Edge-Enhancing Anisotropic Diffusion

The second nonlinear diffusion scheme included in this study is edge-enhancing anisotropic diffusion (EED), which does not only take into account the contrast of an edge, but also its orientation. This is achieved by replacing the scalar-valued diffusivity in (10) by a diffusion tensor:

$$\partial_t I(\mathbf{x};t) = \operatorname{div}\bigl(\mathbf{D}\bigl(\nabla I_\tau\bigr)\nabla I\bigr)(\mathbf{x};t), \tag{12}$$

where, for every $\mathbf{x} \in X$, $\mathbf{D}$ is constructed from the system of orthonormal eigenvectors

$$\begin{aligned} &\mathbf{v}_1 \parallel \nabla I_\tau, \\ &\mathbf{v}_2 \perp \nabla I_\tau, \\ &\mathbf{v}_3 \perp \nabla I_\tau \quad \text{and} \quad \mathbf{v}_3 \perp \mathbf{v}_2, \end{aligned} \tag{13}$$

and corresponding eigenvalues

$$\begin{aligned} \lambda_1 &= D\bigl(\|\nabla I_\tau\|^2\bigr), \\ \lambda_2 &= D(0) = 1, \\ \lambda_3 &= D(0) = 1, \end{aligned} \tag{14}$$

with D as given in (11). This is equivalent to saying $\mathbf{D} = D\bigl(\nabla I_\tau \nabla I_\tau^T\bigr)$, where the argument of D is known as the *structure tensor* [5, 51, 58, 79]. With this choice of $\mathbf{D}$, smoothing along edges is preferred over smoothing across them.

3 Quantification of Vascular Anomalies

Three-dimensional rotational angiography is currently used primarily for visualization and subsequent quantification of carotid stenoses and intracranial aneurysms [2, 32, 48, 72]. In this section, we briefly discuss the measures involved in the quantification of these particular vascular anomalies.

3.1 Quantification of Carotid Stenosis

For the quantification of the degree of stenosis of the internal carotid artery (ICA), many measures have been proposed and applied in the past [25]. Currently, the most frequently used measures are the ones from the North American Symptomatic Carotid Endarterectomy Trial [49,50] and the European Carotid Surgery Trial [15–17], as well as the common carotid (CC) measure [82]. These measures are defined as follows:

$$D_{\mathrm{NASCET}} = 1 - d_{\mathrm{S}}/d_{\mathrm{ICA}}, \tag{15}$$

$$D_{\mathrm{ECST}} = 1 - d_{\mathrm{S}}/d_{\mathrm{O}}, \tag{16}$$

$$D_{\mathrm{CC}} = 1 - d_{\mathrm{S}}/d_{\mathrm{CCA}}, \tag{17}$$

with diameters d_{S}, d_{ICA}, d_{O}, and d_{CCA} as indicated in Figure 1. All three measures involve measuring the luminal diameter at the point of maximum stenosis (d_{S}), but the denominators used to compute the degree of stenosis differ. The NASCET measure involves the diameter (d_{ICA}) of a visible portion of disease-free ICA distal to the stenosis, whereas the ECST measure uses the estimated normal luminal diameter (d_{O}) at the site of the lesion, based on a visual impression of where the normal arterial wall was prior to the development of stenosis. The CC measure involves the diameter (d_{CCA}) of the visible disease-free distal common carotid artery (CCA).

It has been shown that, given fixed percentage ranges to categorize stenosis severity, the differences between results based on the NASCET and ECST measures are considerable and of major clinical importance [60]. Results based on the ECST and CC measures are comparable though, which is explained from the fact that the estimated normal luminal

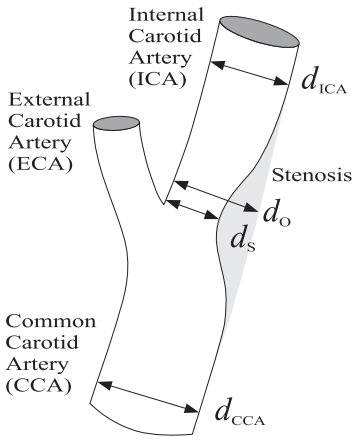

Figure 1. Diameters involved in the different measures for quantification of the degree of carotid stenosis. The stenosis depicted here is located in the internal carotid artery (ICA).

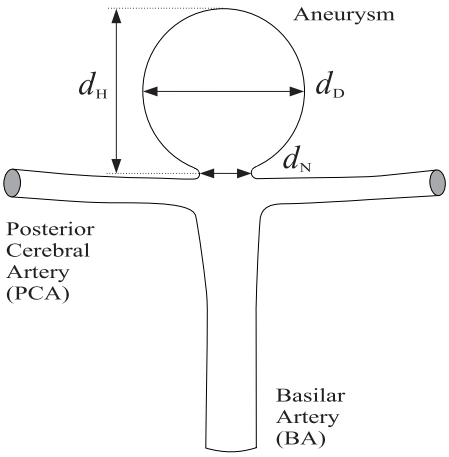

Figure 2. Diameters used for quantification of the size and shape of intracranial saccular aneurysms. The aneurysm depicted here is located at the tip of the basilar artery (BA).

diameter at the site of the lesion is usually approximately equal to the luminal diameter of the CCA [60]. When using the NASCET measure, stenosis may be classified as mild (0%–29%), moderate (30%–69%), or severe (70%–99%). (Corresponding percentage ranges for the ECST and CC measure can be found by making use of the approximately linear or parabolic relationships that have been shown to exist between experimental results of the three measures [19, 60].) It has been demonstrated that surgery is beneficial in symptomatic patients with severe stenosis [49, 53], while the immediate risks of surgery outweigh any potential long-term benefit in patients with mild stenosis. However, there are no definitive conclusions regarding the treatment of patients with moderate stenosis.

3.2 Quantification of Intracranial Aneurysms

For the quantification of intracranial aneurysms, several measures are important. In an attempt to assess the risk of rupture of an aneurysm, early studies have focussed solely on the dome diameter (d_D, see Figure 2). It has been stated that unruptured saccular aneurysms less than 10mm in diameter have a very low probability of subsequent rupture [38, 81]. Later studies have indicated that smaller aneurysms are also associated with a risk of rupture [36, 39, 47, 59, 62, 73, 83, 85]. Some authors have recommended treatment for aneurysms larger than approximately 5mm in diameter [47], while others were unable to find a critical size for unruptured aneurysms below which there is a benign prognosis [39, 59]. Although increased size has been found to relate significantly to risk of rupture [36, 39, 85], the critical size (in terms of dome diameter) is still controversial.

Knowledge of the diameter of the aneurysmal neck (d_N) is important in selecting an appropriate clip in the case of surgical intervention [23]. Neck size has also been shown to be an important factor in predicting successful obliteration of the aneurysmal lumen in the case of endovascular treatment [22, 35]. In the literature, the neck of intracranial saccular aneurysms has been classified into small ($\leqslant$ 4mm) and large ($>$ 4mm) [22, 54, 75]. It has been shown that the probability of achieving complete occlusion is considerably larger for small-necked aneurysms, which is explained from the fact that the smaller the neck, the higher the probability that the mesh of coils bridges across the neck area [22, 31, 33, 75].

Other studies have indicated the possible importance of ratios. For example, the ratio between the neck diameter (d_{N}) and the dome diameter (d_{D}) of the aneurysm may be used as a guideline in deciding between surgical or endovascular treatment [3, 54]. It has also been reported that the outcome of surgery for prolate spheroidal aneurysms (having a small value for the ratio between dome diameter (d_{D}) and dome height (d_{H})) is generally worse than for more spherical lesions [14, 54]. A recent study on the effects of size and shape on the hemodynamics of saccular aneurysms has revealed that the ratio between the height (or depth) of the aneurysm (d_{H}) and the neck diameter (d_{N}) is an important parameter in determining the dynamics of the flow [74]. It was found that aneurysms with depth/neck ratios of more than 1.6 require special care, regardless of actual sizes, because the associated localized low-flow conditions are suspected to induce degeneration of the chemical structure of the aneurysmal wall, leading to increased risk for rupture [74].

4 In-Vitro Experiments

In order to investigate the capabilities of the filtering techniques described in Section 2 to reduce noise and result in improved visualization and quantification of vascular anomalies in 3DRA images, in-vitro experiments were carried out, involving phantoms for which ground truth was available. In this section we briefly describe the phantoms, the image acquisition, and the method of evaluation.

4.1 Phantoms and Image Acquisition

For the experiments concerning the quantification of the degree of carotid stenosis, we used a carotid anthropomorphic vascular phantom (CAVP), modeling an asymmetrical stenosis in the ICA. The experiments concerning the quantification of intracranial aneurysms were carried out on an intracranial anthropomorphic vascular phantom (IAVP), modeling a berry aneurysm located at the tip of the basilar artery (BA). Both phantoms (R. G. Shelley Ltd., North York, Ontario, Canada) represent average dimensions of the corresponding vascular structures in the human body [21, 67]. The relevant diameters in the CAVP were (cf. Figure 1): $d_{\mathrm{S}} = 1.68$mm, $d_{\mathrm{ICA}} = 5.60$mm, and $d_{\mathrm{CCA}} = 8.00$mm, which are equal to the ones mentioned by Smith *et al.* [67]. In the IAVP, the relevant diameters were (cf. Figure 2): $d_{\mathrm{N}} = 2.6$mm and $d_{\mathrm{D}} = 12.9$mm. We note that the latter diameters were obtained from the manufacturer and may differ from the ones originally described by Fahrig *et al.* [21].

Three-dimensional images of each of the phantoms were obtained as follows. First, the phantom was filled with contrast material Ultravist-300 (Schering, Weesp, the Netherlands), diluted to 50% with Natriumchloride 0.9% (Fresenius, 's-Hertogenbosch, the Netherlands). Next, the rotational angiography facility of an Integris V3000 C-arm imaging system (Philips Medical Systems, Best, the Netherlands) was used to acquire a sequence of 100 X-ray angiography images (see Figure 3 for examples) at different views by automatic rotation of the C-arm over 180 degrees in about eight seconds. All projection images were acquired with a 20cm image intensifier, having a matrix size of 512×512 pixels, and a grey-level resolution of 10 bits per pixel. The X-ray intensity was 60kV, 15ms exposure per image. Finally, a modification of Feldkamp's cone-beam algorithm [30] was applied to generate 3D reconstructions at two different resolutions: $128 \times 128 \times 128$ voxels of $0.6 \times 0.6 \times 0.6\mathrm{mm}^3$ (hereafter referred to as the low-resolution reconstruction), and $256 \times 256 \times 256$ voxels of $0.3 \times 0.3 \times 0.3\mathrm{mm}^3$ (referred to as the high-resolution reconstruction). In both cases, the grey-level resolution was 16 bits per voxel.

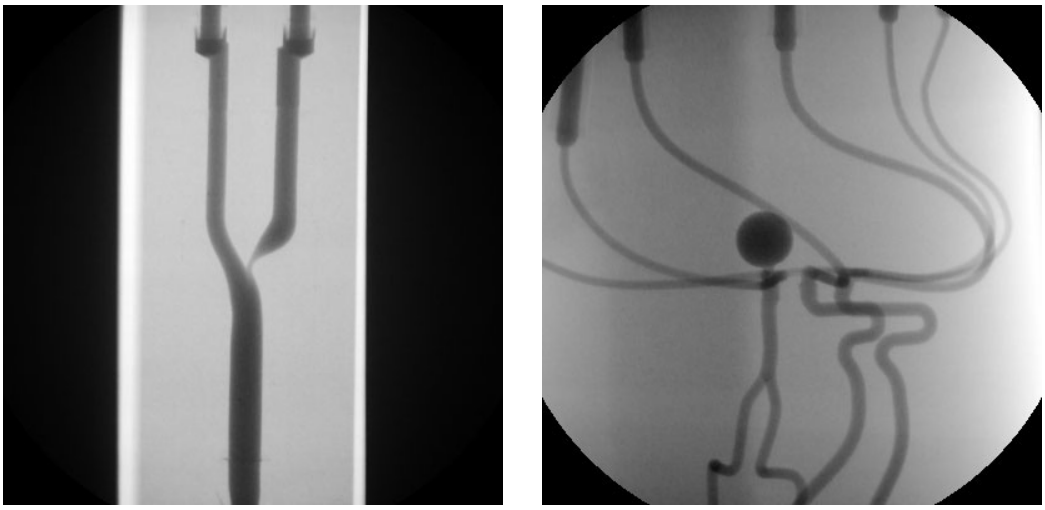

Figure 3. Sample X-ray projection images taken from the rotational angiography runs of the CAVP (left) and the IAVP (right). These images are meant to give an impression of the morphology and complexity of the modeled vasculature.

4.2 Method of Evaluation

We first investigated the capabilities of the filtering techniques to reduce background noise while retaining vessel contrast as much as possible. In order to quantify this, we used the contrast-to-noise ratio (CNR), which is defined as the squared difference between the mean grey-value within a vessel segment of interest and the mean grey-value in a neighboring background region, divided by the variance of the grey-values in the latter region [1, 13]:

$$\mathrm{CNR} = \left(\frac{\langle I \rangle_{\mathcal{V}} - \langle I \rangle_{\mathcal{B}}}{\sigma_{\mathcal{B}}} \right)^2 , \tag{18}$$

where $\mathcal{V}$ and $\mathcal{B}$ denote vessel and background regions, respectively. Since a given filtering technique can be expected to behave similarly in all parts of the background in the phantom images, we selected only a single background region in each of the images. However, the effects of any technique on the local contrast may be dependent on the size and shape of the vessel segment of interest. Therefore, the contrast was measured separately for the CCA, the ICA, and the point of maximum stenosis in the images of the CAVP, and for the dome and neck in the images of the IAVP.

The CNR was measured as a function of "evolution time". This variable, t, is explicitly present in the RPM and EED scheme (see (10) and (12), respectively) and, together with the temporal step-size Δt, determines the number of iterations of the discretized version of the differential equation involved. In the GF scheme (when implemented by spatial convolution), this variable is related to the standard deviation of the Gaussian kernel by $t = \sigma^2/2$, as explained in Section 2.2. In order to obtain an "evolution time" for the UF scheme, we used that same expression, with σ the standard deviation of the kernel defined in (3). This implies that $t = m^2/24$, where m is a discrete variable for which we took values of $3, 5, 7, 9$, and 11. In order to allow for a direct comparison of the results of the techniques, the CNR measurements for the GF, RPM, and EED scheme were carried out at the corresponding evolution times $t = 0.375$, 1.042, 2.042, 3.375, and 5.042. The measurements were also performed in the original 3DRA images ($t = 0.0$).

Next, we investigated the effects of the different noise reduction techniques on the quantification of the vascular anomalies discussed in Section 3. Concerning the quantification of the degree of internal carotid stenosis, the experiments were limited to determining D_{NASCET} and D_{CC}, which implied measuring d_{S}, d_{ICA}, and d_{CCA} (cf. (15), (17), and Figure 1). According to the specifications of the CAVP (Section 4.1), these measurements should yield $D_{\text{NASCET}} = 70\%$ and $D_{\text{CC}} = 79\%$. The ECST measure was not determined, since it requires the normal luminal diameter at the point of maximum stenosis, d_{O}, which cannot be measured in the phantom images used in this study. As for the quantification of intracranial aneurysms, the experiments were limited to measuring d_{N} and d_{D} (cf. Figure 2 and Section 4.1). The dome height, d_{H}, was not determined, since it would require user interaction to indicate the transition between the dome and the neck of the aneurysm.

The vessel diameters were measured as a function of both evolution time (t) and a user-controlled threshold parameter (θ). Concerning the former, we used the same values as in the CNR measurements. As explained in the introduction (Section 1), a threshold parameter is currently used in practice to separate relevant (vascular) structures from non-relevant (noise and other background) structures in the volume or surface renderings, on the base of which quantification takes place. In order to be able to use acquisition independent values for this parameter, the phantom images were "normalized" in such a way that the average background intensity was 0.0, and the average intensity within the vessels of interest 1.0. The measurements were carried out for thresholds ranging from 0.1 to 0.9, with a step size of 0.02. Together with the ground-truth values, the results of these experiments allowed for the assessment of both accuracy and robustness to threshold selection of quantitative measurements, and their dependency on the filter strength.

The actual determination of luminal diameters was done as follows. For each of the vessel segments involved, a perpendicular cut-plane was determined interactively. In this plane, grey-level profiles passing through the center of the vessel in question were analyzed. Given a profile, the luminal diameter was defined as the distance between the points on either side of the center of the vessel along that profile at which the grey-level passed through the user-defined threshold level θ. The location of these points was determined with a precision of 1/100th of a voxel by trilinear interpolation. In order to increase the robustness of the measurements, we used 10 profiles, equally divided over 360 degrees within the cut-plane, and the average of the resulting diameters was taken as the final diameter. This was done for all segments, except for the neck of the aneurysm, which was the only segment in the phantoms that did not have a circular cross section. Therefore, we used only a single profile for the neck diameter measurements. Since in our IAVP only the (smallest) neck diameter in the anterior/posterior direction was specified (d_{N}), the single profile was taken in that direction.

Finally, we looked at the visual (qualitative) effects of the different noise reduction techniques. These concerned the apparent (not measured) dimensions of the vascular anomalies in 3D visualizations of the filtered 3DRA datasets and their dependency on the user-controlled threshold parameter, as well as the apparent smoothness of the vascular structures in these visualizations. These effects may be important when 3D visualizations are used for navigational purposes, such as *e.g.* in (future) endovascular interventional applications. In order to give an impression of these effects, both exo- and endovascular surface renderings were generated. All surface renderings were obtained by using a modification of the Phong light model [63], which separates reflected light into an ambient component (factor k_a), a diffuse component (factor k_d), and a specular component (factor k_s). In all renderings, we used the following values: $k_a = 0.2$, $k_d = 0.4$, and $k_s = 0.4$.

We note that, apart from the time parameter, the RPM and EED schemes have two additional parameters: the noise scale σ_n and the contrast parameter ζ. The former causes the gradient-magnitude computations to be relatively insensitive to variations at scales smaller than σ_n. Since the aim was to preserve the entire vasculature as much as possible, and particular (segments of) vessels were quite small (*e.g.* the point of maximum stenosis!), we chose to use a small value for this parameter, *viz.*, $\sigma_n = 0.5$. The contrast parameter ζ acts as a threshold against which local gradient magnitudes are compared in deciding between destruction or preservation of the underlying image structure. Using the same arguments, we concluded that the value of this parameter should be chosen as small as possible. After initial experimentation with RPM and EED applied to the normalized phantom images, we found that $\zeta = 0.05$ yields satisfactory results for both schemes; much larger values resulted in additional blurring of the vessel walls, while too much noise was preserved with much smaller values. The just mentioned values for the noise and contrast parameter were kept fixed in all experiments.

5 Results

The results of the CNR measurements carried out in the 3DRA images of the CAVP and IAVP are presented in Figures 4 and 5. From the plots it follows that, for the range of evolution times considered in these experiments, the four schemes UF, GF, RPM, and EED reduced noise equally well in vessel segments with a large luminal diameter, where "large" has to be taken relative to the voxel size of the image. This applies to the CCA and the dome of the aneurysm in both the high- and low-resolution reconstruction of the CAVP and IAVP, respectively, and the ICA in the high-resolution reconstruction of the CAVP. For the segments with smaller diameters, *viz.*, the point of maximum stenosis and the neck of the aneurysm in both the high- and low-resolution reconstruction of, respectively, the CAVP and IAVP, as well as the ICA in the low-resolution reconstruction of the CAVP, the nonlinear filtering techniques (RPM and EED) outperformed the linear techniques (UF and GF) for larger evolution times.

The results of the experiments concerning the effects of the different noise reduction techniques on carotid stenosis and intracranial aneurysm quantification are presented in Figures 6–8. We note that the results of the D_{CC} measurements are not given here, since they were very similar to those of the D_{NASCET} measurements. The plots show that for the linear techniques (UF and GF), the dependency of the measurements on the user-controlled threshold parameter (θ) increased dramatically (in both the high- and low-resolution reconstructions of the CAVP and IAVP) as the filtering was made stronger (larger t). The RPM scheme, on the other hand, had a negligible influence on this dependency, irrespective of resolution or evolution time. The effects of the EED scheme on the user-dependency were found to be negligible only in the high-resolution reconstructions. Concerning the low-resolution reconstructions, the effects of EED were most noticeable in the quantification of the degree of stenosis.

Finally, examples of exo- and endovascular surface renderings generated from the high-resolution 3DRA images of the CAVP and IAVP after application of the different noise reduction techniques, are presented in Figures 9–12. The renderings show close-up 3D visualizations of the vascular anomalies and give a visual impression of the effects of the techniques on the smoothness of the vessel walls and the changes in the apparent dimensions of the anomalies when varying the user-controlled threshold parameter. The renderings support the findings of the quantification experiments: the linear techniques

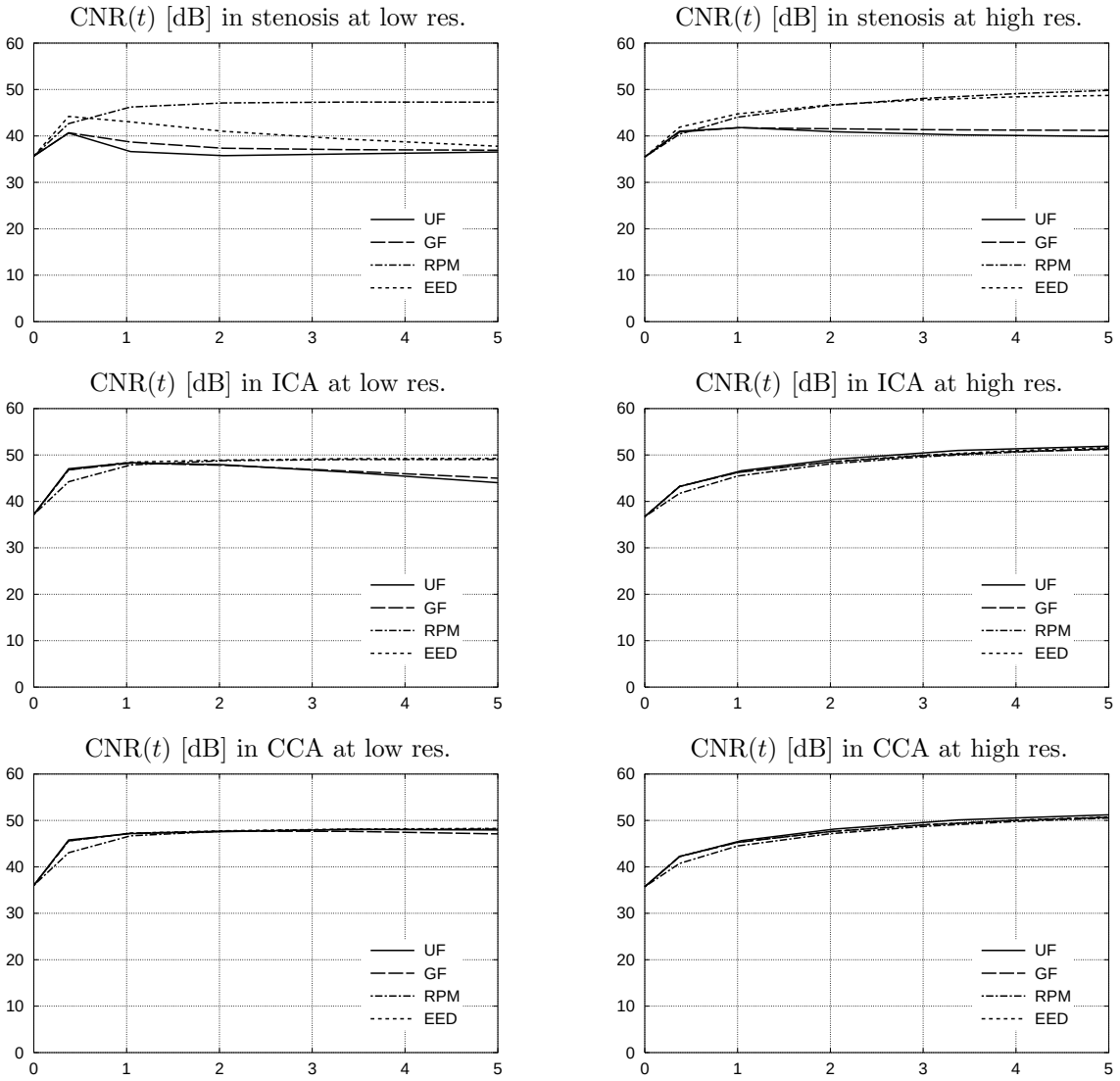

Figure 4. Contrast-to-noise ratio (CNR) as a function of evolution time (t) for the four noise reduction techniques described in Section 2, measured in the stenosis (top row), ICA (middle row), and CCA (bottom row) in the low- (left column) and high-resolution (right column) 3DRA reconstruction of the CAVP.

(UF and GF) increased the user-dependency of the (measured or observed) dimensions of the anomalies. In contrast, the negative effects of the nonlinear techniques (RPM and EED) in the high-resolution 3DRA reconstructions were negligible. Notice, however, that the smoothness of the vessel walls was considerably improved by EED, while most of the noise in these edge regions was retained by RPM.

6 Discussion

Techniques for the reduction of noise in digital images have been developed and reported since the 1970s. Concerning the preservation of edges, early evaluation studies [10, 45, 84] already indicated the superiority of nonlinear techniques such as median filtering or

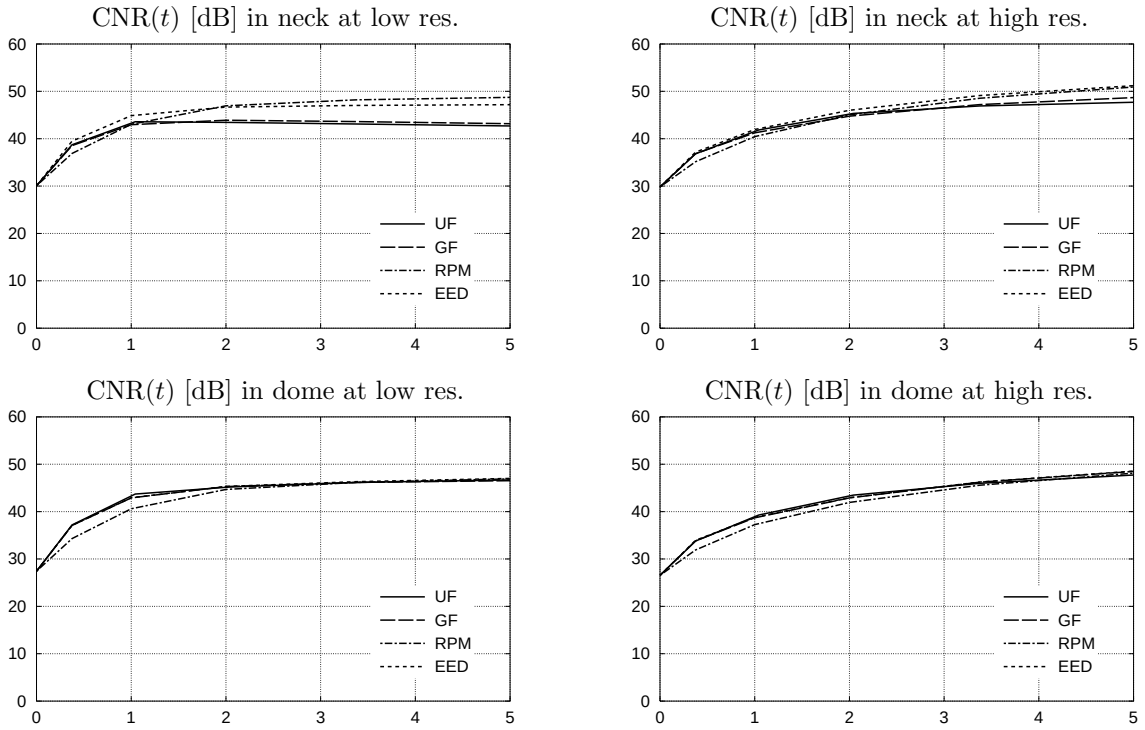

Figure 5. Contrast-to-noise ratio (CNR) as a function of evolution time (t) for the four noise reduction techniques described in Section 2, measured in the neck (top row) and dome (bottom row) of the aneurysm in the low- (left column) and high-resolution (right column) 3DRA reconstruction of the IAVP.

adaptive K-nearest neighbor averaging over linear techniques. However, these nonlinear techniques may easily result in a loss of resolution due to their tendency to suppress fine details, as has been pointed out in the field of medical imaging by *e.g.* Gerig *et al.* [28]. Developments in the past decade have resulted in new approaches to noise reduction based on nonlinear diffusion filtering [8, 51, 56, 77–80]. These techniques were explicitly designed to preserve edges and fine details, and to overcome the major drawbacks of conventional filtering techniques, such as the inevitable trade-off between localization accuracy and detectability, which occurs *e.g.* in edge detection based on linear operators [7], or the difficulty of scale selection or multi-scale integration, which occurs in recently reported approaches to vessel-enhancement filtering [9, 11, 12, 27, 44, 52, 57, 61]. Several nonlinear diffusion schemes have already been applied successfully in biological and medical imaging [4, 26, 28, 43, 55, 65, 66, 69]. Evaluations of such techniques for the present application have not been reported previously, however.

The experimental results presented in the previous section show that the four noise reduction techniques considered in this study (UF, GF, RPM, and EED) were equally capable of increasing the CNR in vessel segments with a relatively large luminal diameter. This can be explained from the fact that in the experiments, the vessel regions $\mathcal{V}$ (see Section 4.2) were taken rather small (typically a few voxels in all three dimensions) and close to the center of the lumen. As a consequence, for the range of evolution times considered, linear filtering (UF or GF) did not result in a blurring of the vessel walls to the extent that it reduced the mean grey-level within regions $\mathcal{V}$ in segments with a luminal diameter larger than about 10 voxels. Furthermore, the nonlinear techniques (RPM and

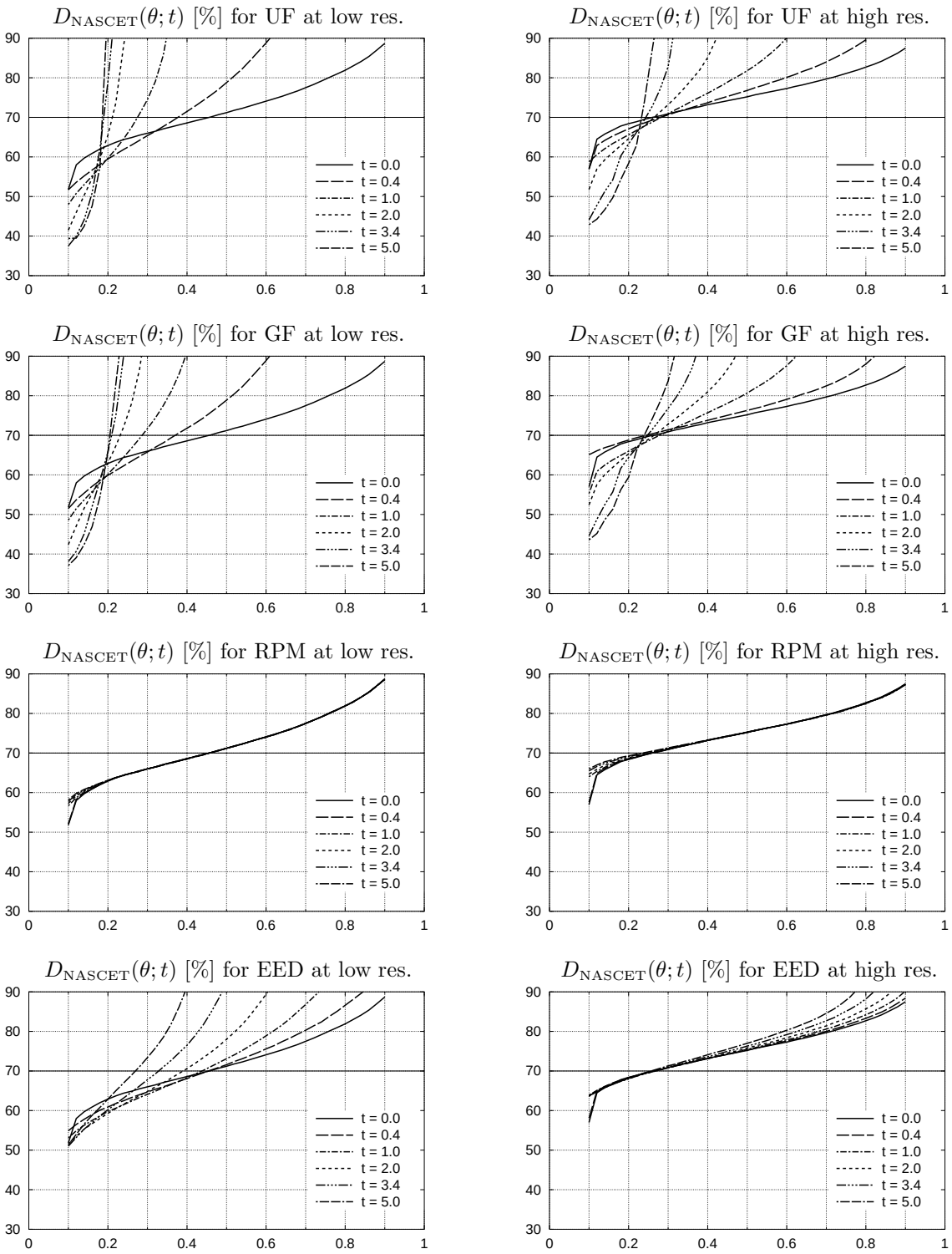

Figure 6. The degree of internal carotid stenosis (D_{NASCET}) as a function of the user-controlled threshold (θ) and evolution time (t) for the four noise reduction techniques: UF (first row), GF (second row), RPM (third row), and EED (last row), as measured in the low- (left column) and high-resolution (right column) 3DRA reconstruction of the CAVP. The horizontal line at $D_{\mathrm{NASCET}} = 70\%$ indicates the true value.

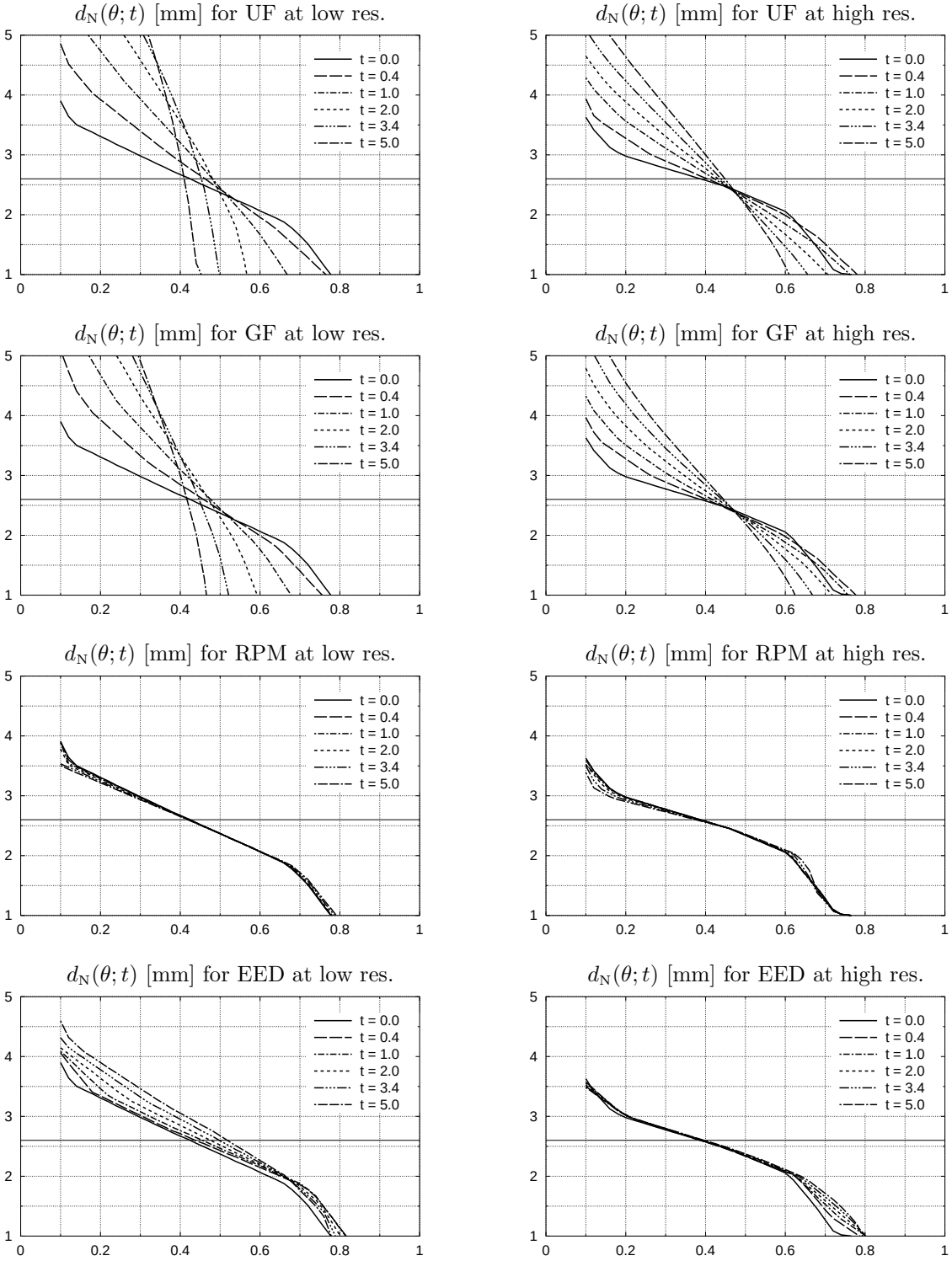

Figure 7. The diameter of the neck of the aneurysm (d_N) as a function of the user-controlled threshold (θ) and evolution time (t) for the four noise reduction techniques: UF (first row), GF (second row), RPM (third row), and EED (last row), as measured in the low- (left column) and high-resolution (right column) 3DRA reconstruction of the IAVP. The horizontal line at $d_N = 2.6$mm indicates the true value.

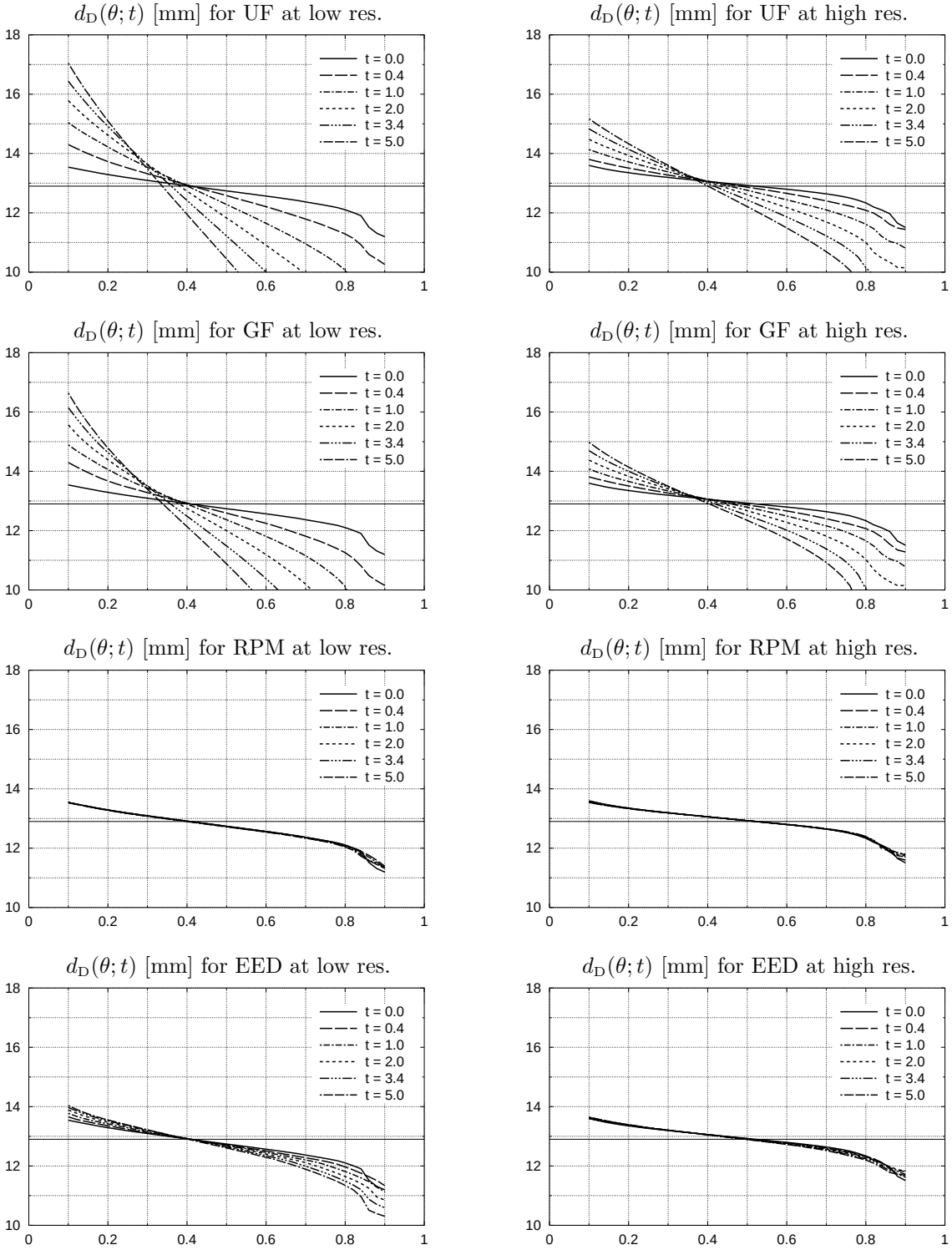

Figure 8. The diameter of the dome of the aneurysm (d_D) as a function of the user-controlled threshold (θ) and evolution time (t) for the four noise reduction techniques: UF (first row), GF (second row), RPM (third row), and EED (last row), as measured in the low- (left column) and high-resolution (right column) 3DRA reconstruction of the IAVP. The horizontal line at $d_D = 12.9$mm indicates the true value.

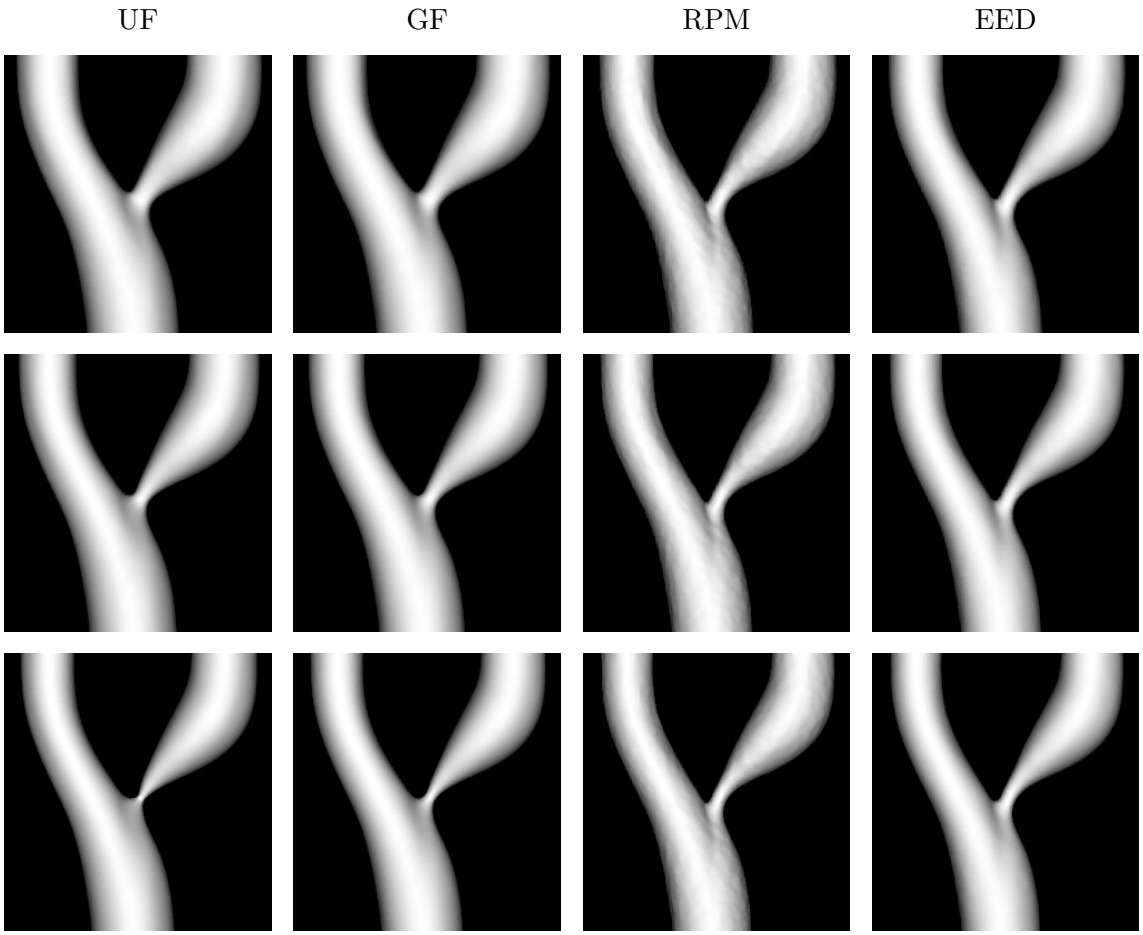

Figure 9. Exovascular surface renderings illustrating the effects of the different noise reduction techniques on the smoothness of the vessel walls and the apparent degree of stenosis when varying the user-controlled threshold parameter. The renderings show a close-up of the stenosis and its related vessels (ICA, ECA, and CCA; cf. Figure 1), and were generated from the high-resolution 3DRA image of the CAVP after application of, respectively, UF (left column), GF (middle-left column), RPM (middle-right column), and EED (right column), at evolution time $t = 2.042$. The thresholds used were, respectively, $\theta = 0.2$ (top row), $\theta = 0.3$ (middle row), and $\theta = 0.4$ (bottom row).

EED) approached GF in these non-edge regions—(10) and (12) both converge to (9) for $\|\nabla I_\tau\| \ll \zeta$. In the vessel segments with smaller diameters, the contrast-reducing effects of linear filtering were noticeable at much earlier evolution times. This explains the lagging CNR(t) curves of the linear techniques compared to those of the nonlinear techniques in these cases (see again the plots in Figures 4 and 5), where the time of parting is determined not only by the local luminal diameter, but also by the morphology of the surrounding vasculature. The CNR measurement results also show that, of the nonlinear techniques, RPM was superior to EED regarding the preservation of local contrast in vessel segments with very small diameters (in these experiments only the point of maximum stenosis in the low-resolution reconstruction of the CAVP, where the local luminal diameter was less than three voxels). This is due to the fact that near edges, blurring is completely inhibited with RPM, while the anisotropic behavior of EED still allows for some blurring in the plane orthogonal to the local gradient.

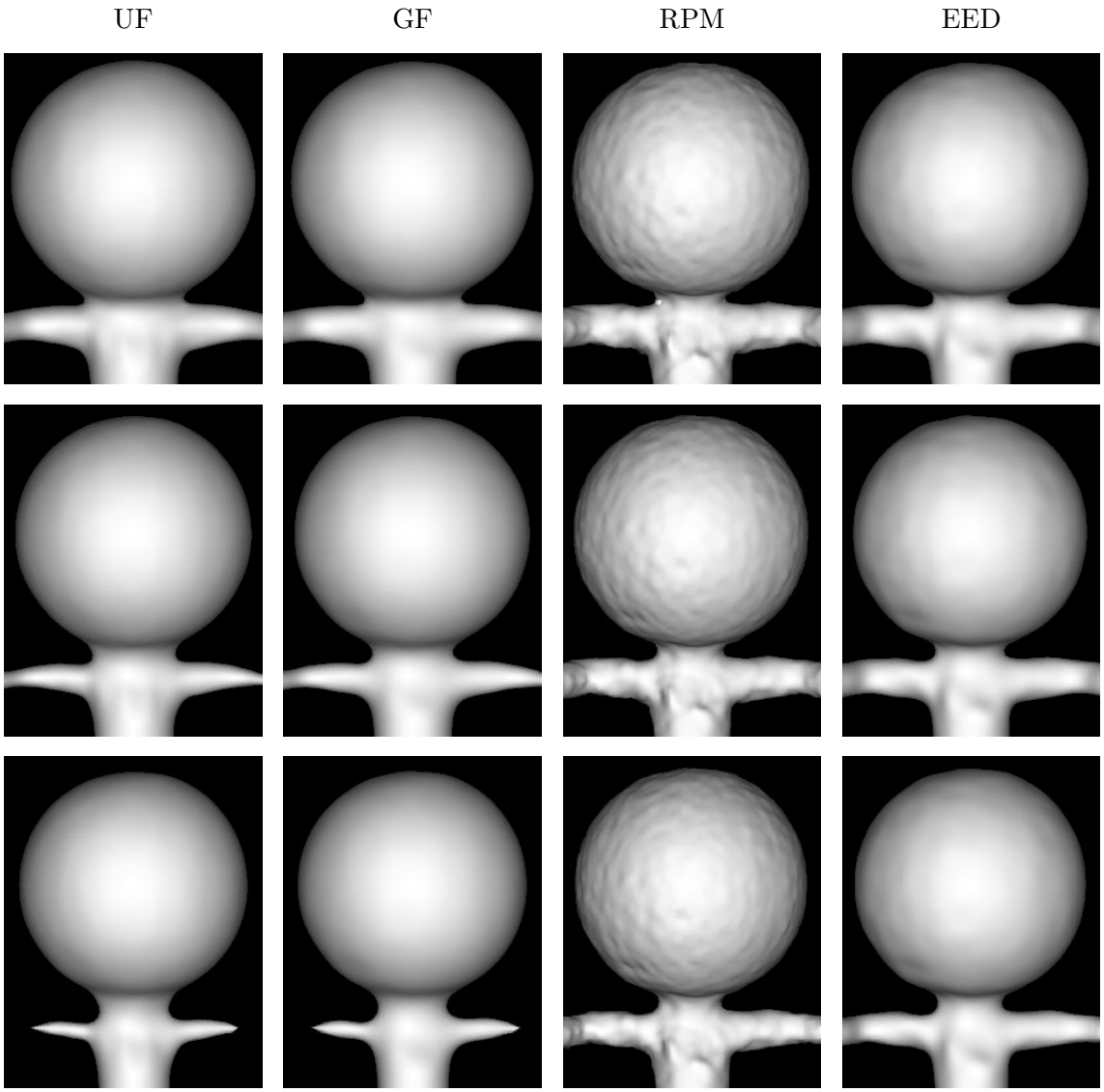

Figure 10. Exovascular surface renderings illustrating the effects of the different noise reduction techniques on the smoothness of the vessel walls and the apparent size of especially the neck of the aneurysm, when varying the user-controlled threshold parameter. The renderings show a close-up of the neck and the dome of the aneurysm and its related vessels (the BA and both PCAs; cf. Figure 2), and were generated from the high-resolution 3DRA image of the IAVP after application of, respectively, UF (left column), GF (middle-left column), RPM (middle-right column), and EED (right column), at evolution time $t = 2.042$. The thresholds used were, respectively, $\theta = 0.3$ (top row), $\theta = 0.4$ (middle row), and $\theta = 0.5$ (bottom row).

Whereas the CNR measurements concerned the behavior of the noise reduction techniques in the background and the interior of vessels, the diameter measurements were intended to study their performance at the transitions from background to vessel interior. The plots in Figures 6–8 reveal that the differences between UF and GF were negligible in that respect: the increase in the dependency of the measurements on the user-controlled threshold θ was comparable with the two techniques. However, as expected, this increase was considerably less in the high-resolution reconstructions compared to the low-resolution

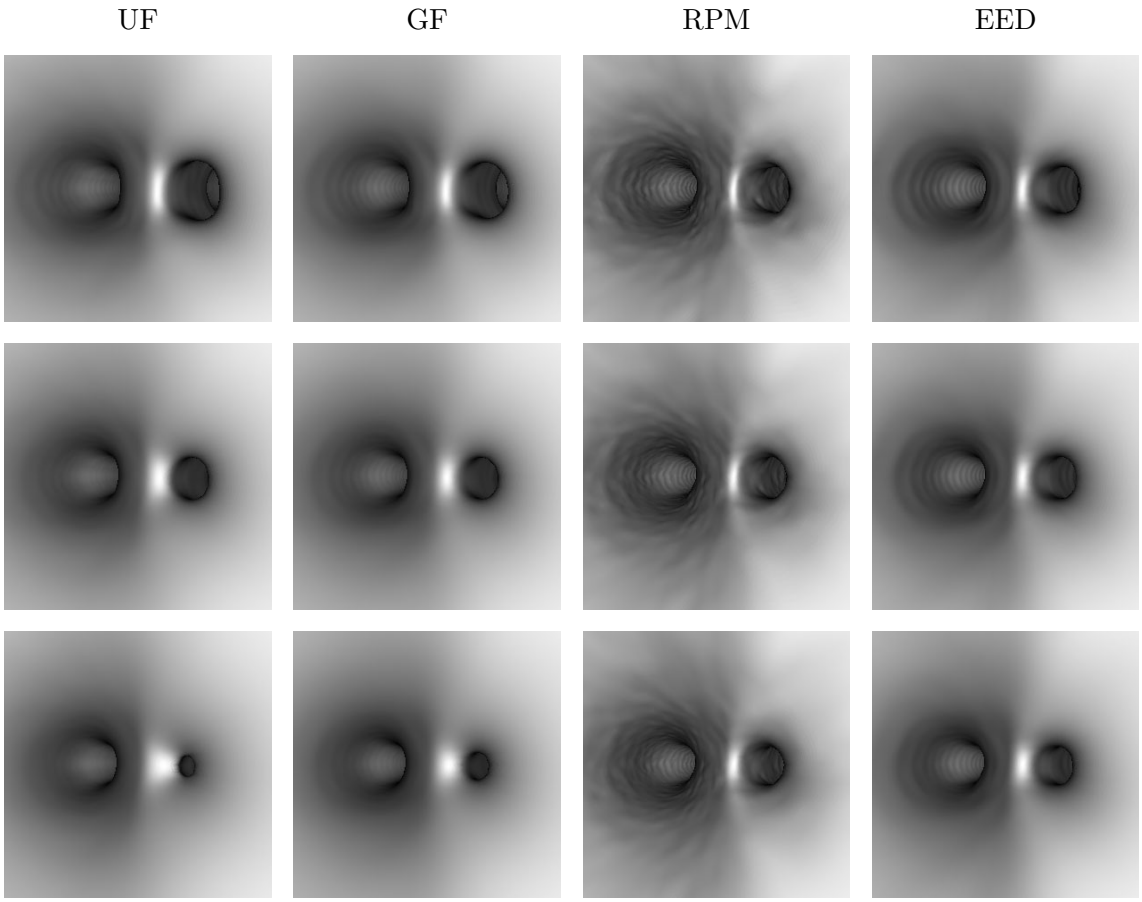

Figure 11. Endovascular surface renderings illustrating the effects of the different noise reduction techniques on the smoothness of the vessel walls and the apparent degree of stenosis when varying the user-controlled threshold parameter. The renderings show the ECA (left passage) and the stenosis in the ICA (right passage), viewed from within the CCA, and were generated from the high-resolution 3DRA image of the CAVP after application of, respectively, UF (left column), GF (middle-left column), RPM (middle-right column), and EED (right column), at evolution time $t = 2.042$. The thresholds used were, respectively, $\theta = 0.2$ (top row), $\theta = 0.3$ (middle row), and $\theta = 0.4$ (bottom row).

reconstructions. For example, in the low-resolution reconstruction of the CAVP resulting from UF at $t = 1.042$, changing the threshold from $\theta = 0.2$ to $\theta = 0.4$ implied an increase in D_{NASCET} from 60% to well over 90%. In the high-resolution reconstruction, on the other hand, the increase was only from about 66% to about 77%. Since $D_{\text{NASCET}} = 70\%$ is usually considered an important threshold in deciding between intervention or no intervention [25, 49, 53, 60], we may conclude that UF and GF put high demands on the resolution at which user-controlled measurements are to be carried out. In contrast, RPM did not increase the user-dependency of the measurements, and the plots show that this dependency was somewhat less in the high-resolution reconstructions. The small amount of anisotropic blurring allowed by the EED scheme near edges did not have appreciable effects on the user-dependency of the measurements in the high-resolution reconstructions, in which all diameters were larger than about five voxels. It is important to note here that although RPM and EED did not *in*crease the user-dependency of the measurements for vessels of this size, they did not *de*crease it either, from which we have to conclude that

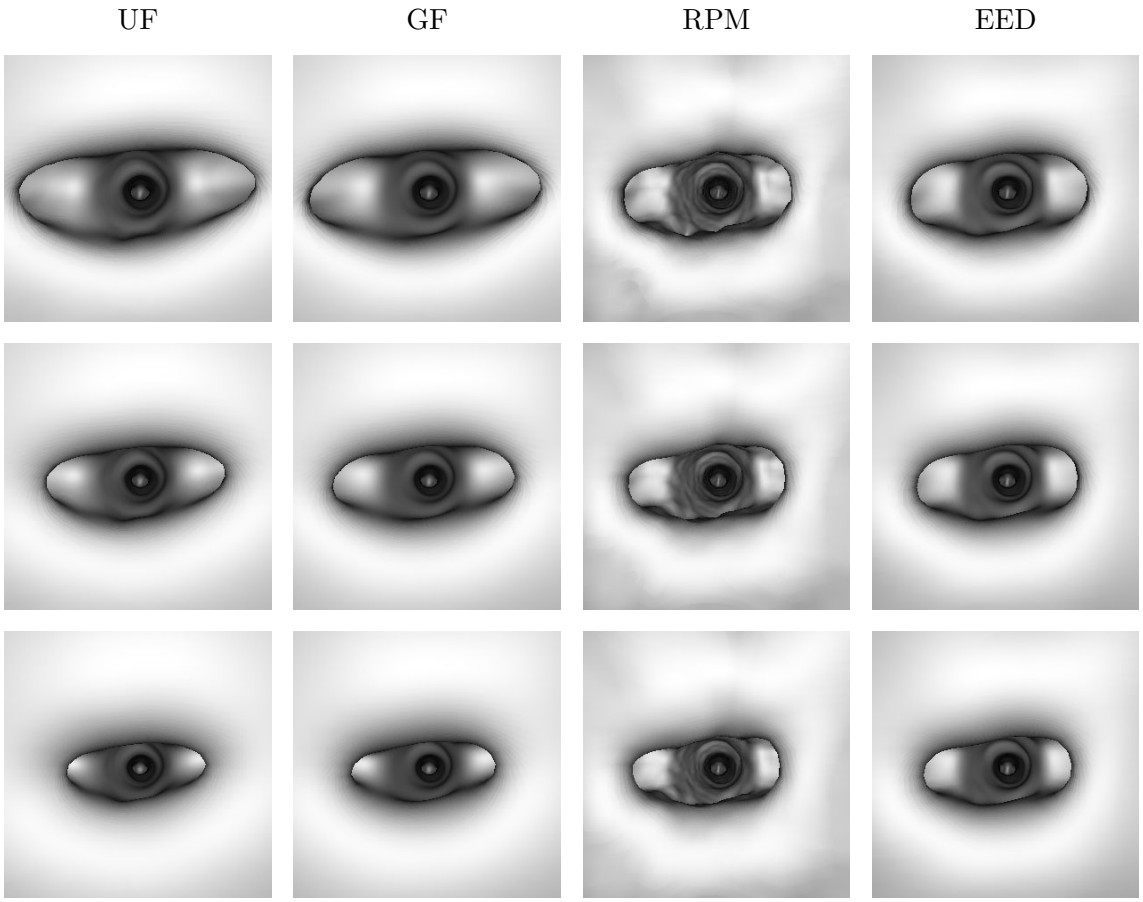

Figure 12. Endovascular surface renderings illustrating the effects of the different noise reduction techniques on the smoothness of the vessel walls and the apparent size of the neck of the aneurysm, when varying the user-controlled threshold parameter. The renderings show the neck and the BA (straight-through passage) and PCAs (left and right passages) behind it, viewed from within the dome of the aneurysm, and were generated from the high-resolution 3DRA image of the IAVP after application of, respectively, UF (left column), GF (middle-left column), RPM (middle-right column), and EED (right column), at evolution time $t = 2.042$. The thresholds used were, respectively, $\theta = 0.3$ (top row), $\theta = 0.4$ (middle row), and $\theta = 0.5$ (bottom row).

with the measurement technique employed in this study there is in fact no need to apply such schemes for the purpose of quantification. Finally, the relatively large effects on the user-dependency in the low-resolution reconstruction of the CAVP in the case of EED can be ascribed primarily to the blurring effects at the point of maximum stenosis, where the local diameter was considerably less than five voxels.

Notice that in these quantification experiments, we measured only diameters. This is justified by the fact that, except for the neck of the aneurysm, all vessel segments in the 3DRA phantom images were known to have circular cross sections. Moreover, determining diameters fits in with the currently used measures for quantification of vascular anomalies (see Section 3). The reason that these diameter-based measures have become so established is that, for many decades, quantification has been based on 2D projective X-ray angiography, notably DSA. In fact, DSA is still considered by many the gold standard for this purpose. In principle, 3DRA allows us to express important measures such as the

degree of carotid stenosis in terms of cross-sectional areas rather than diameters. This would indeed be more realistic, since in practice vessels do not necessarily have circular cross sections and, in principle, the blood volume passing through a vessel per unit time is dependent on its cross-sectional area. It is important to note, however, that the observed effects of filtering on quantification will be much more severe when using areas instead of diameters, due to the quadratic relation that exists between these two.

The sample exo- and endovascular surface renderings in Figures 9–12 clearly illustrate that noise was heavily reduced with UF and GF, but the increased user-dependency easily resulted in a misleading rendering of the dimensions of vessel segments with relatively small diameters (mainly the point of maximum stenosis in Figures 9 and 11, and the PCAs and connected neck of the aneurysm in Figures 10 and 12). The conceptual differences between the two nonlinear techniques, mentioned previously in the discussion of the quantification results, are also manifest in these figures. Although the user-dependency of the apparent vascular dimensions was considerably less with both techniques, the anisotropic behavior of EED resulted in smoother vessel walls, while most of the noise remained after application of RPM. Notice that the renderings in these figures were generated from the high-resolution reconstructions, and at time $t = 2.042$. Clearly, the observed effects were much more pronounced in the low-resolution reconstructions and/or at larger t. One might argue that the negative effects of linear filtering could be confined by keeping t low. However, this would also limit the improvement in CNR (see again Figures 4 and 5). It is to be expected that clinical 3DRA images require even larger t, since these images do not only contain reconstruction noise, but also unwanted variations due to surrounding tissue. The effects of the different techniques applied to an example clinical dataset are shown in Figure 13. The renderings show once again that EED is better at smoothing vessel walls, at the risk of losing vessels with very small diameters.

Overall, the results of the experiments suggest that for reconstructions with a sufficiently high resolution, EED is most suitable: the increase in the user-dependency of quantifications and visualizations is considerably less than with UF or GF, and EED is better at reducing noise at the vessel walls than RPM. The sub-optimal performance of EED in vessel segments with very small luminal diameters (occurring at lower resolutions), is most probably due to the fact that the amount of blurring in the plane orthogonal to a local gradient is equal in all directions—the eigenvalues λ_2 and λ_3 of the diffusion tensor are equal, see Section 2.4. We suspect that in order for EED to work adequately also in these cases, it is necessary to make a distinction between the directions corresponding to minimal and maximal curvature; especially in vessel segments with small diameters, the behavior of EED in these directions can be quite different. However, this would require the use of second-order information (Hessian), which is not incorporated in the present scheme. Early experiments with curvature-based anisotropic diffusion schemes [41] have shown promising results, but more elaborate evaluations are required to determine the clinical implications.

Other disadvantages of the current implementation of EED are its memory requirements and its relatively high computational cost. Concerning the former, EED requires an amount of memory equal to nine times the size of the original image. With RPM and UF/GF, respectively, only four and two times the size of the original image is required. If computations are carried out with floating-point precision, this implies that in order to process an image of size $256 \times 256 \times 256$ voxels, the amount of memory required by EED, RPM, and UF/GF, would be about 605MB, 270MB, and 135MB, respectively. For an image of size $128 \times 128 \times 128$ voxels, this would be about 76MB, 34MB, and 17MB, respectively. Considering the fact that the amount of memory available in current worksta-

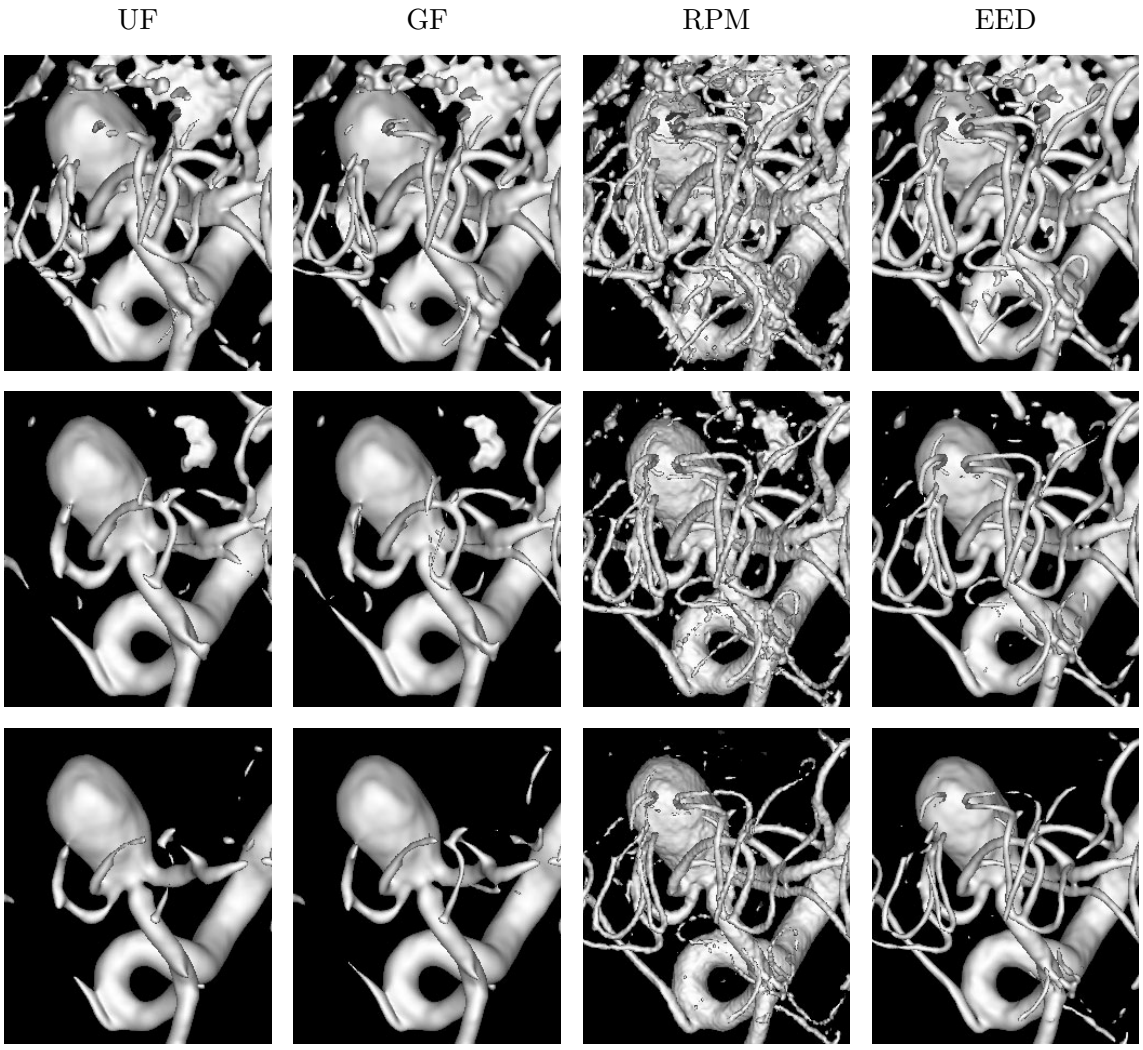

Figure 13. Surface renderings illustrating the effects of the different noise reduction techniques in the case of a clinical 3DRA dataset of a 57-year old patient with a giant aneurysm at the splitting of the middle cerebral artery. The renderings were generated after application of, respectively, UF (left column), GF (middle-left column), RPM (middle-right column), and EED (right column), at evolution time $t = 2.042$. The thresholds used were, respectively, $\theta = 0.3$ (top row), $\theta = 0.4$ (middle row), and $\theta = 0.5$ (bottom row).

tions is usually 256MB or 512MB, we conclude that application of EED is as yet limited to small-sized reconstructions. Regarding computational cost, the major difference between the linear and the nonlinear schemes is that the former require only a single application of the corresponding convolution equation in order to arrive at any given time t (UF allows only particular discrete times though), while the latter usually require repeated application of the discretized version of the differential equation involved. The number of iterations is then determined by the temporal step-size, Δt. In order to guarantee stability with explicit or Euler-forward implementations, it is required that $\Delta t < 1/(2N)$, with N the dimensionality of the dataset to which the schemes are applied [77, 79, 80]. In the case of RPM, the use of additive operator splitting results in a much more efficient implementation [80]. However, such an approach is less beneficial in the case of anisotropic diffusion.

The use of a diffusion tensor (EED) instead of a scalar-valued diffusivity (RPM) further increases the number of operations to be carried out. We observed that with a step-size of $\Delta t = 1/8$, EED required about eight minutes in order to arrive at $t = 2.0$ with a dataset of size $128 \times 128 \times 128$ voxels, while the other schemes required only a fraction of that time. The computation times were measured on an Octane workstation (Silicon Graphics, De Meern, the Netherlands) with one 195MHz MIPS R10000 processor and 256MB main memory (instruction and data cache size both 32KB), after reconstruction. For comparison we mention that on the same machine, the time required for the reconstruction of a volume of mentioned size is less than five minutes.

7 Conclusions

We investigated the effects of linear (UF, GF) and nonlinear (RPM, EED) noise reduction techniques on the visualization and quantification of vascular anomalies (carotid stenosis and intracranial aneurysms) in 3DRA images. Several experiments were carried out on low-resolution ($0.6 \times 0.6 \times 0.6\text{mm}^3$ voxels) and high-resolution ($0.3 \times 0.3 \times 0.3\text{mm}^3$ voxels) 3DRA reconstructions of a CAVP and an IAVP, modeling an asymmetrical stenosis in the ICA and a berry aneurysm located at the tip of the BA, respectively. The results of CNR measurements indicated that RPM and EED are better capable of reducing background noise while preserving local contrast than UF or GF. In addition, the increase in the dependency of diameter measurements on the user-controlled threshold was shown to be considerably less with RPM and EED compared to UF or GF. In both type of experiments, we observed that in vessel segments with very small luminal diameters (a few voxels), RPM performs somewhat better than EED. However, for the range of diameters considered in this study, the differences between the two techniques were found to be negligible in high-resolution reconstructions. Finally, exo- and endovascular surface renderings of the phantom images after processing with the different techniques revealed that RPM does not improve the quality of visualizations near vessel walls. Therefore we conclude that, as far as the trade-off between accuracy of quantification and quality of visualization is concerned, EED is to be preferred for high-resolution reconstructions. However, considering the relatively high demands of this scheme in terms of memory and computation time, RPM may be considered a useful alternative where these are decisive factors.

Acknowledgments

The research described in this paper was carried out at the Image Sciences Institute, University Medical Center Utrecht (UMCU), the Netherlands, and was financially supported by the Netherlands Ministry of Economic Affairs. The authors are grateful to Wilma Pauw (UMCU) for assisting them in acquiring the rotational X-ray angiography runs, as well as to Rolf Suurmond and John op de Beek (Philips Medical Systems, Best, the Netherlands) for providing them with the necessary software and know-how to reconstruct the 3DRA datasets used in this study.

References

[1] I. E. Abdou & W. K. Pratt, "Quantitative Design and Evaluation of Enhancement / Thresholding Edge Detectors", *Proceedings of the IEEE*, vol. 67, no. 5, 1979, pp. 753–763.

[2] R. Anxionnat, S. Bracard, J. Macho, E. Da Costa, R. Vaillant, L. Launay, Y. Trousset, R. Romeas, L. Picard, "3D Angiography: Clinical Interest. First Applications in Interventional Neuroradiology", *Journal of Neuroradiology*, vol. 25, no. 4, 1998, pp. 251–262.

[3] G. Bavinzski, B. Richling, A. Gruber, M. Killer, D. Levy, "Endosaccular Occlusion of Basilar Artery Bifurcation Aneurysms using Electrically Detachable Coils", *Acta Neurochirurgica*, vol. 134, no. 3/4, 1995, pp. 184–189.

[4] F. J. Beekman, E. T. P. Slijpen, W. J. Niessen, "Selection of Task-Dependent Diffusion Filters for the Post-Processing of SPECT Images", *Physics in Medicine and Biology*, vol. 43, no. 6, 1998, pp. 1713–1730.

[5] J. Bigün, G. H. Granlund, J. Wiklund, "Multidimensional Orientation Estimation with Applications to Texture Analysis and Optical Flow", *IEEE Transactions on Pattern Analysis and Machine Intelligence*, vol. 13, no. 8, 1991, pp. 775–790.

[6] Z. Bosanac, R. J. Miller, M.Jain, "Rotational Digital Subtraction Carotid Angiography: Technique and Comparison with Static Digital Subtraction Angiography", *Clinical Radiology*, vol. 53, no. 9, 1998, pp. 682–687.

[7] J. F. Canny, "A Computational Approach to Edge Detection", *IEEE Transactions on Pattern Analysis and Machine Intelligence*, vol. 8, no. 6, 1986, pp. 679–698.

[8] F. Catté, P.-L. Lions, J.-M. Morel, T. Coll, "Image Selective Smoothing and Edge Detection by Nonlinear Diffusion", *SIAM Journal on Numerical Analysis*, vol. 29, no. 1, 1992, pp. 182–193.

[9] H. Chen & J. Hale, "An Algorithm for MR Angiography Image Enhancement", *Magnetic Resonance in Medicine*, vol. 33, no. 4, 1995, pp. 534–540.

[10] R. T. Chin & C.-L. Yeh, "Quantitative Evaluation of Some Edge-Preserving Noise-Smoothing Techniques", *Computer Vision, Graphics and Image Processing*, vol. 23, no. 1, 1983, pp. 67–91.

[11] Y. P. Du & D. L. Parker, "Vessel Enhancement Filtering in Three-Dimensional MR Angiography", *Journal of Magnetic Resonance Imaging*, vol. 5, no. 3, 1995, pp. 353–359.

[12] Y. P. Du & D. L. Parker, "Vessel Enhancement Filtering in Three-Dimensional MR Angiograms using Long-Range Signal Correlation", *Journal of Magnetic Resonance Imaging*, vol. 7, no. 2, 1997, pp. 447–450.

[13] Y. P. Du, D. L. Parker, W. L. Davis, D. D. Blatter, "Contrast-to-Noise-Ratio Measurements in Three-Dimensional Magnetic Resonance Angiography", *Investigative Radiology*, vol. 28, no. 11, 1993, pp. 1004–1009.

[14] K. Ebina, T. Shimizu, M. Sohma, T. Iwabuchi, "Clinico-Statistical Study on Morphological Risk Factors of Middle Cerebral Artery Aneurysms", *Acta Neurochirurgica*, vol. 106, no. 3/4, 1990, pp. 153–159.

[15] ECST Collaborative Group, "MRC European Carotid Surgery Trial: Interim Results for Symptomatic Patients with Severe (70-99%) or with Mild (0-29%) Carotid Stenosis", *The Lancet*, vol. 337, no. 8752, 1991, pp. 1235–1243.

[16] ECST Collaborative Group, "Endarterectomy for Moderate Symptomatic Carotid Stenosis: Interim Results from the MRC European Carotid Surgery Trial", *The Lancet*, vol. 347, no. 9015, 1996, pp. 1591–1593.

[17] ECST Collaborative Group, "Randomised Trial of Endarterectomy for Recently Symptomatic Carotid Stenosis: Final Results of the MRC European Carotid Surgery Trial (ECST)", *The Lancet*, vol. 351, no. 9113, 1998, pp. 1379–1387.

[18] O. E. H. Elgersma, P. C. Buijs, A. F. J. Wüst, Y. van der Graaf, B. C. Eikelboom, W. P. T. M. Mali, "Maximum Internal Carotid Arterial Stenosis: Assessment with Rotational Angiography versus Conventional Intraarterial Digital Subtraction Angiography", *Radiology*, vol. 213, no. 3, 1999, pp. 777–783.

[19] M. Eliasziw, R. F. Smith, N. Singh, D. W. Holdsworth, A. J. Fox, H. J. M. Barnett, "Further Comments on the Measurement of Carotid Stenosis from Angiograms", *Stroke*, vol. 25, no. 12, 1994, pp. 2445–2449.

[20] R. Fahrig, A. J. Fox, S. Lownie, D. W. Holdsworth, "Use of a C-Arm System to Generate True Three-Dimensional Computed Rotational Angiograms: Preliminary In Vitro and In Vivo Results", *American Journal of Neuroradiology*, vol. 18, no. 8, 1997, pp. 1507–1514.

[21] R. Fahrig, H. Nikolov, A. J. Fox, D. W. Holdsworth, "A Three-Dimensional Cerebrovascular Flow Phantom", *Medical Physics*, vol. 26, no. 8, 1999, pp. 1589–1599.

[22] A. Fernandez Zubillaga, G. Guglielmi, F. Viñuela, G. R. Duckwiler, "Endovascular Occlusion of Intracranial Aneurysms with Electrically Detachable Coils: Correlation of Aneurysm Neck Size and Treatment Results", *American Journal of Neuroradiology*, vol. 15, no. 5, 1994, pp. 815–820.

[23] C. L. Fink, R. E. Flandry, R. A. Pratt, C. B. Early, "A Comparative Study of Performance Characteristics of Cerebral Aneurysm Clips", *Surgical Neurology*, vol. 11, no. 3, 1979, pp. 179–186.

[24] L. M. J. Florack, *Image Structure*, vol. 10 of *Computational Imaging and Vision*, Kluwer Academic Publishers, Dordrecht, 1997.

[25] A. J. Fox, "How to Measure Carotid Stenosis", *Radiology*, vol. 186, no. 2, 1993, pp. 316–318.

[26] A. S. Frangakis & R. Hegerl, "Nonlinear Anisotropic Diffusion in Three-Dimensional Electron Microscopy", in *Scale-Space Theories in Computer Vision*, M. Nielsen, P. Johansen, O. F. Olsen, J. Weickert (eds.), vol. 1682 of *Lecture Notes in Computer Science*, Springer-Verlag, Berlin, Germany, 1999, pp. 386–397.

[27] A. F. Frangi, W. J. Niessen, K. L. Vincken, M. A. Viergever, "Multiscale Vessel Enhancement Filtering", in *Medical Image Computing and Computer-Assisted Intervention (MICCAI'98)*, W. M. Wells, A. Colchester, S. Delp (eds.), vol. 1496 of *Lecture Notes in Computer Science*, Springer-Verlag, Berlin, Germany, 1998, pp. 130–137.

[28] G. Gerig, O. Kübler, R. Kikinis, F. A. Jolesz, "Nonlinear Anisotropic Filtering of MRI Data", *IEEE Transactions on Medical Imaging*, vol. 11, no. 2, 1992, pp. 221–232.

[29] R. C. Gonzalez & P. Wintz, *Digital Image Processing*, no. 13 in Applied Mathematics and Computation, Addison-Wesley, Reading, MA, 1977.

[30] M. Grass, R. Koppe, E. Klotz, R. Proksa, M. H. Kuhn, H. Aerts, J. op de Beek, R. Kemkers, "Three-Dimensional Reconstruction of High Contrast Objects using C-Arm Image Intensifier Projection Data", *Computerized Medical Imaging and Graphics*, vol. 23, no. 6, 1999, pp. 311–321.

[31] G. Guglielmi, F. Viñuela, G. Duckwiler, J. Dion, P. Lylyk, A. Berenstein, C. Strother, V. Graves, V. Halbach, D. Nichols, N. Hopkins, R. Ferguson, I. Sepetka, "Endovascular Treatment of Posterior Circulation Aneurysms by Electrothrombosis using Electrically Detachable Coils", *Journal of Neurosurgery*, vol. 77, no. 4, 1992, pp. 515–524.

[32] J. F. Heautot, E. Chabert, Y. Gandon, S. Croci, R. Romeas, R. Campagnolo, B. Chereul, J. M. Scarabin, M. Carsin, "Analysis of Cerebrovascular Diseases by a New 3-Dimensional Computerised X-Ray Angiography System", *Neuroradiology*, vol. 40, no. 4, 1998, pp. 203–209.

[33] S. K. Hilal & R. A. Solomon, "Endovascular Treatment of Aneurysms with Coils", *Journal of Neurosurgery*, vol. 76, no. 2, 1992, pp. 337–339.

[34] D. J. Hoff, M. C. Wallace, K. G. terBrugge, F. Gentili, "Rotational Angiography Assessment of Cerebral Aneurysms", *American Journal of Neuroradiology*, vol. 15, no. 10, 1994, pp. 1945–1948.

[35] J. K. A. Hope, J. V. Byrne, A. J. Molyneux, "Factors Influencing Successful Angiographic Occlusion of Aneurysms Treated by Coil Embolization", *American Journal of Neuroradiology*, vol. 20, no. 3, 1999, pp. 391–399.

[36] T. Inagawa & A. Hirano, "Ruptured Intracranial Aneurysms: An Autopsy Study of 133 Patients", *Surgical Neurology*, vol. 33, no. 2, 1990, pp. 117–123.

[37] B. Jähne, *Digital Image Processing. Concepts, Algorithms, and Scientific Applications*, Springer-Verlag, Berlin, 1991.

[38] M. Jomin, F. Lesoin, G. Lozes, A. Fawaz, L. Villette, "Surgical Prognosis of Unruptured Intracranial Arterial Aneurysms: Report of 50 Cases", *Acta Neurochirurgica*, vol. 84, no. 3/4, 1987, pp. 85–88.

[39] S. Juvela, M. Porras, O. Heiskanen, "Natural History of Unruptured Intracranial Aneurysms: A Long-Term Follow-Up Study", *Journal of Neurosurgery*, vol. 79, no. 2, 1993, pp. 174–182.

[40] J. J. Koenderink, "The Structure of Images", *Biological Cybernetics*, vol. 50, 1984, pp. 363–370.

[41] K. Krissian, G. Malandain, N. Ayache, "Directional Anisotropic Diffusion Applied to Segmentation of Vessels in 3D Images", in *Scale-Space Theory in Computer Vision*, B. ter Haar Romeny, L. Florack, J. Koenderink, M. Viergever (eds.), vol. 1252 of *Lecture Notes in Computer Science*, Springer-Verlag, Berlin, Germany, 1997, pp. 345–348.

[42] T. Lindeberg, *Scale-Space Theory in Computer Vision*, The Kluwer International Series in Engineering and Computer Science, Kluwer Academic Publishers, Dordrecht, 1994.

[43] M. Loew, J. Rosenman, J. Chen, "A Clinical Tool for Enhancement of Portal Images", in *Medical Imaging: Image Processing*, M. H. Loew (ed.), vol. 2167 of *Proceedings of SPIE*, The International Society for Optical Engineering, Bellingham, Washington, USA, 1994, pp. 543–550.

[44] C. Lorenz, I.-C. Carlsen, T. M. Buzug, C. Fassnacht, J. Weese, "Multi-Scale Line Segmentation with Automatic Estimation of Width, Contrast and Tangential Direction in 2D and 3D Medical Images", in *CVRMed-MRCAS'97*, J. Troccaz, E. Grimson, R. Mösges (eds.), vol. 1205 of *Lecture Notes in Computer Science*, Springer-Verlag, Berlin, Germany, 1997, pp. 233–242.

[45] G. A. Mastin, "Adaptive Filters for Digital Image Noise Smoothing: An Evaluation", *Computer Vision, Graphics and Image Processing*, vol. 31, no. 1, 1985, pp. 103–121.

[46] E. Meijering, W. Niessen, J. Weickert, M. Viergever, "Evaluation of Diffusion Techniques for Improved Vessel Visualization and Quantification in Three-Dimensional Rotational Angiography", in *Medical Image Computing and Computer-Assisted Intervention (MICCAI-2001)*, W. J. Niessen & M. A. Viergever (eds.), Springer-Verlag, Berlin, 2001, pp. 177–185.

[47] K. Mizoi, T. Yoshimoto, Y. Nagamine, T. Kayama, K. Koshu, "How to Treat Incidental Cerebral Aneurysms: A Review of 139 Consecutive Cases", *Surgical Neurology*, vol. 44, no. 8, 1995, pp. 114–121.

[48] J. Moret, R. Kemkers, J. op de Beek, R. Koppe, E. Klotz, M. Grass, "3D Rotational Angiography: Clinical Value in Endovascular Treatment", *Medicamundi*, vol. 42, no. 3, 1998, pp. 8–14.

[49] NASCET Collaborators, "Beneficial Effect of Carotid Endarterectomy in Symptomatic Patients with High-Grade Carotid Stenosis", *The New England Journal of Medicine*, vol. 325, no. 7, 1991, pp. 445–453.

[50] NASCET Steering Committee, "North American Symptomatic Carotid Endarterectomy Trial. Methods, Patient Characteristics, and Progress", *Stroke*, vol. 22, no. 5, 1991, pp. 711–720.

[51] M. Nitzberg & T. Shiota, "Nonlinear Image Filtering with Edge and Corner Enhancement", *IEEE Transactions on Pattern Analysis and Machine Intelligence*, vol. 14, no. 8, 1992, pp. 826–833.

[52] M. M. Orkisz, C. Bresson, I. E. Magnin, O. Champin, P. C. Douek, "Improved Vessel Visualization in MR Angiography by Nonlinear Anisotropic Filtering", *Magnetic Resonance in Medicine*, vol. 37, no. 6, 1997, pp. 914–919.

[53] M. Paciaroni, M. Eliasziw, L. J. Kappelle, J. W. Finan, G. G. Ferguson, H. J. Barnett, "Medical Complications Associated with Carotid Endarterectomy", *Stroke*, vol. 30, no. 9, 1999, pp. 1759–1763.

[54] L. Parlea, R. Fahrig, D. W. Holdsworth, S. P. Lownie, "An Analysis of the Geometry of Saccular Intracranial Aneurysms", *American Journal of Neuroradiology*, vol. 20, no. 6, 1999, pp. 1079–1089.

[55] E. Payot, R. Guillemaud, Y. Trousset, F. Preteux, "An Adaptive and Constrained Model for 3D X-Ray Vascular Reconstruction", in *Three-Dimensional Image Reconstruction in Radiation and Nuclear Medicine*, P. Grangeat & J.-L. Amans (eds.), vol. 4 of *Computational Imaging and Vision*, Kluwer Academic Publishers, Dordrecht, the Netherlands, 1996, pp. 47–57.

[56] P. Perona & J. Malik, "Scale-Space and Edge Detection using Anisotropic Diffusion", *IEEE Transactions on Pattern Analysis and Machine Intelligence*, vol. 12, no. 7, 1990, pp. 629–639.

[57] R. Poli & G. Valli, "An Algorithm for Real-Time Vessel Enhancement and Detection", *Computer Methods and Programs in Biomedicine*, vol. 52, no. 1, 1997, pp. 1–22.

[58] A. R. Rao & B. G. Schunck, "Computing Oriented Texture Fields", *CVGIP: Graphical Models and Image Processing*, vol. 53, no. 2, 1991, pp. 157–185.

[59] J. Rosenørn & V. Eskesen, "Does a Safe Size-Limit Exist for Unruptured Intracranial Aneurysms?", *Acta Neurochirurgica*, vol. 121, no. 3/4, 1993, pp. 113–118.

[60] P. M. Rothwell, R. J. Gibson, J. Slattery, R. J. Sellar, C. P. Warlow, "Equivalence of Measurements of Carotid Stenosis. A Comparison of Three Methods on 1001 Angiograms", *Stroke*, vol. 25, no. 12, 1994, pp. 2435–2439.

[61] Y. Sato, S. Nakajima, N. Shiraga, H. Atsumi, S. Yoshida, T. Koller, G. Gerig, R. Kikinis, "Three-Dimensional Multi-Scale Line Filter for Segmentation and Visualization of Curvilinear Structures in Medical Images", *Medical Image Analysis*, vol. 2, no. 2, 1998, pp. 143–168.

[62] W. I. Schievink, D. G. Piepgras, F. P. Wirth, "Rupture of Previously Documented Small Asymptomatic Saccular Intracranial Aneurysms. Report of Three Cases", *Journal of Neurosurgery*, vol. 76, no. 6, 1992, pp. 1019–1024.

[63] C. Schlick, "A Fast Alternative to Phong's Specular Model", in *Graphics Gems*, P. S. Heckbert (ed.), vol. IV of *The Graphics Gems Series*, Academic Press, Boston, MA, 1994, Ch. VI.1, pp. 385–387.

[64] B. A. Schueler, A. Sen, H.-H. Hsiung, R. E. Latchaw, X. Hu, "Three-Dimensional Vascular Reconstruction with a Clinical X-Ray Angiography System", *Academic Radiology*, vol. 4, no. 10, 1997, pp. 693–699.

[65] J. Sijbers, A. J. den Dekker, A. van der Linden, T. M. Verhoye, D. van Dyck, "Adaptive Anisotropic Noise Filtering for Magnitude MR Data", *Magnetic Resonance Imaging*, vol. 17, no. 10, 1999, pp. 1533–1539.

[66] J. Sijbers, P. Scheunders, M. Verhoye, A. van der Linden, D. van Dyck, E. Raman, "Watershed-Based Segmentation of 3D MR Data for Volume Quantization", *Magnetic Resonance Imaging*, vol. 15, no. 6, 1997, pp. 679–688.

[67] R. F. Smith, B. K. Rutt, A. J. Fox, R. N. Rankin, D. W. Holdsworth, "Geometric Characterization of Stenosed Human Carotid Arteries", *Academic Radiology*, vol. 3, no. 11, 1996, pp. 898–911.

[68] J. Sporring, M. Nielsen, L. Florack, P. Johansen (eds.), *Gaussian Scale-Space Theory*, vol. 8 of *Computational Imaging and Vision*, Kluwer Academic Publishers, Dordrecht, 1997.

[69] E. Steen & B. Olstad, "Scale-Space and Boundary Detection in Ultrasonic Imaging using Nonlinear Signal-Adaptive Anisotropic Diffusion", in *Medical Imaging: Image Processing*, M. H. Loew (ed.), vol. 2167 of *Proceedings of SPIE*, The International Society for Optical Engineering, Bellingham, Washington, USA, 1994, pp. 116–127.

[70] B. M. ter Haar Romeny (ed.), *Geometry-Driven Diffusion in Computer Vision*, vol. 1 of *Computational Imaging and Vision*, Kluwer Academic Publishers, Dordrecht, 1994.

[71] G. Tommasini, A. Camerini, A. Gatti, G. Derchi, A. Bruzzone, C. Vecchio, "Panoramic Coronary Angiography", *Journal of the American College of Cardiology*, vol. 31, no. 4, 1998, pp. 871–877.

[72] Y. Trousset, R. Vaillant, L. Launay, J.-M. Obadia, N. Pivet, R. Anxionnat, L. Picard, "A Fully Automated System for Three-Dimensional X-Ray Angiography", in *Computer Assisted Radiology and Surgery (CARS'99)*, H. U. Lemke, M. W. Vannier, K. Inamura, A. G. Farman (eds.), vol. 1191 of *International Congress Series*, Elsevier, Amsterdam, 1999, pp. 39–43.

[73] H. Ujiie, K. Sato, H. Onda, A. Oikawa, M. Kagawa, K. Takakura, N. Kobayashi, "Clinical Analysis of Incidentally Discovered Unruptured Aneurysms", *Stroke*, vol. 24, no. 12, 1993, pp. 1850–1856.

[74] H. Ujiie, H. Tachibana, O. Hiramatsu, A. L. Hazel, T. Matsumoto, Y. Ogasawara, H. Nakajima, T. Hori, K. Takakura, F. Kajiya, "Effects of Size and Shape (Aspect Ratio) on the Hemodynamics of Saccular Aneurysms: A Possible Index for Surgical Treatment of Intracranial Aneurysms", *Neurosurgery*, vol. 45, no. 1, 1999, pp. 119–129.

[75] F. Viñuela, G. Duckwiler, M. Mawad, "Guglielmi Detachable Coil Embolization of Acute Intracranial Aneurysm: Perioperative Anatomical and Clinical Outcome in 403 Patients", *Journal of Neurosurgery*, vol. 86, no. 3, 1997, pp. 475–482.

[76] J. Weickert, "A Review of Nonlinear Diffusion Filtering", in *Scale-Space Theory in Computer Vision*, B. ter Haar Romeny, L. Florack, J. Koenderink, M. Viergever (eds.), vol. 1252 of *Lecture Notes in Computer Science*, Springer-Verlag, Berlin, 1997, pp. 3–28.

[77] J. Weickert, *Anisotropic Diffusion in Image Processing*, B. G. Teubner, Stuttgart, 1998.

[78] J. Weickert, "Coherence-Enhancing Diffusion Filtering", *International Journal of Computer Vision*, vol. 31, no. 2/3, 1999, pp. 111–127.

[79] J. Weickert, "Nonlinear Diffusion Filtering", in *Handbook on Computer Vision and Applications,* vol. 2: *Signal Processing and Pattern Recognition*, B. Jähne, H. Haußecker, P. Geißler (eds.), Academic Press, San Diego, CA, 1999, Ch. 15, pp. 423–450.

[80] J. Weickert, B. M. ter Haar Romeny, M. A. Viergever, "Efficient and Reliable Schemes for Nonlinear Diffusion Filtering", *IEEE Transactions on Image Processing*, vol. 7, no. 3, 1998, pp. 398–410.

[81] D. O. Wiebers, J. P. Whisnant, T. M. Sundt, W. M. O'Fallon, "The Significance of Unruptured Intracranial Saccular Aneurysms", *Journal of Neurosurgery*, vol. 66, no. 1, 1987, pp. 23–29.

[82] M. A. Williams & A. N. Nicolaides, "Predicting the Normal Dimensions of the Internal and External Carotid Arteries from the Diameter of the Common Carotid", *European Journal of Vascular Surgery*, vol. 1, no. 2, 1987, pp. 91–96.

[83] H. R. Winn, W. S. Almaani, S. L. Berga, J. A. Jane, A. E. Richardson, "The Long-Term Outcome in Patients with Multiple Aneurysms. Incidence of Late Hemorrhage and Implications for Treatment of Incidental Aneurysms", *Journal of Neurosurgery*, vol. 59, no. 4, 1983, pp. 642–651.

[84] W.-Y. Wu, M.-J. J. Wang, C.-M. Liu, "Performance Evaluation of Some Noise Reduction Techniques", *CVGIP: Graphical Models and Image Processing*, vol. 54, no. 2, 1992, pp. 134–146.

[85] N. Yasui, S. Magarisawa, A. Suzuki, H. Nishimura, T. Okudera, T. Abe, "Subarachnoid Hemorrhage Caused by Previously Diagnosed, Previously Unruptured Intracranial Aneurysms: A Retrospective Analysis of 25 Cases", *Neurosurgery*, vol. 39, no. 6, 1996, pp. 1096–1100.